

## Supporting Information

### **Chromophore-Protein Interplay During the Phytochrome Photocycle Revealed by Step-Scan FTIR Spectroscopy**

Janne A. Ihalainen<sup>1,\*</sup>, Emil Gustavsson<sup>2,†</sup>, Lea Schroeder<sup>3,†</sup>, Serena Donnini<sup>1</sup>, Heli Lehtivuori<sup>4</sup>, Linnéa Isaksson<sup>2</sup>, Christian Thöing<sup>3</sup>, Vaibhav Modi<sup>5</sup>, Oskar Berntsson<sup>2</sup>, Brigitte Stucki-Buchli<sup>1</sup>, Alli Liukkonen<sup>1</sup>, Heikki Häkkänen<sup>1</sup>, Elina Kalenius<sup>5</sup>, Sebastian Westenhoff<sup>2,\*</sup>, Tilman Kottke<sup>3,\*</sup>

1) University of Jyväskylä, Nanoscience Center, Department of Biological and Environmental Science, Jyväskylä, 40014 Finland

2) University of Gothenburg, Department of Chemistry and Molecular Biology, Gothenburg, 40530 Sweden

3) Bielefeld University, Physical and Biophysical Chemistry, Universitätsstr. 25, 33615 Bielefeld, Germany

4) University of Jyväskylä, Nanoscience Center, Department of Physics, Jyväskylä, 40014 Finland

5) University of Jyväskylä, Nanoscience Center, Department of Chemistry, Jyväskylä, 40014 Finland

\*Corresponding authors; email: [janne.ihalainen@jyu.fi](mailto:janne.ihalainen@jyu.fi), [westenho@chem.gu.se](mailto:westenho@chem.gu.se), [tilman.kottke@uni-bielefeld.de](mailto:tilman.kottke@uni-bielefeld.de)

†These authors contributed equally to this work

## SI Materials and Methods

### Protein Expression and Purification

#### ***In Vivo* Production of the PAS-GAF-PHY Fragment of a Bacteriophytochrome.**

The dimeric and monomeric (mutations for monomeric form: F145S, L311E, and L314E)<sup>1</sup> PAS-GAF-PHY fragments of a bacteriophytochrome were expressed with (His)<sub>6</sub>-tag in *Escherichia coli* strain BL21(DE3) as previously described<sup>2</sup>.

***In Vivo* Production of Labeled Monomeric PAS-GAF-PHY Apoprotein.** Uniformly <sup>13</sup>C<sup>15</sup>N-labeled PAS-GAF-PHY monomer apoprotein was expressed with (His)<sub>6</sub>-tag in *Escherichia coli* strain BL21(DE3) as previously described<sup>2</sup>, with the following modifications: Expression cultures were grown in a standard M9 minimal media with 150 µg/ml ampicillin. Carbon source was u-<sup>13</sup>C<sub>6</sub> glucose, nitrogen source was <sup>15</sup>NH<sub>4</sub>Cl (Cambridge Isotope Laboratories). Cultures were incubated at 37°C and 220 rpm until they reached OD<sub>600</sub>=0.7-0.8. They were induced with 1mM IPTG, temperature was lowered to 28°C and incubated for 22h after which the cells were harvested by centrifugation.

***In Vitro* Production of Aspartic Acid-Labeled PAS-GAF-PHY Protein.** Aspartic acid-labeled PAS-GAF-PHY dimeric apoprotein was expressed *in vitro* as previously described<sup>3</sup>, with the following modifications: L-Aspartic acid was interchanged for <sup>13</sup>C<sub>4</sub>-labeled L-aspartic acid (Cambridge Isotope Laboratories). 20mM aminooxyacetic acid was added to prevent the degradation of aspartic acid to glutamic acid and subsequent scrambling of the isotopes.

**Purification of Labeled and Non-Labeled Monomeric and Dimeric PAS-GAF-PHY.** After lysis, the sample was ultracentrifuged and incubated on ice in the dark overnight, with 10x molar excess of biliverdin. The resulting holoprotein was subjected to Ni<sup>2+</sup>-affinity purification (30 mM Tris-HCl, pH 8.0, 50 mM NaCl) with an elution buffer containing 300 mM imidazole. A subsequent size exclusion chromatography was performed with 30 mM Tris-HCl, pH 8.0. Purified protein was concentrated to 20 mg/mL and flash frozen in liquid nitrogen. The labeling was confirmed by ESI-MS (Figure S4).

**Purification of Aspartic Acid-Labeled PAS-GAF-PHY.** After *in vitro* expression the sample was centrifuged and diluted 1:1 with buffer (30 mM Tris-HCl, pH 8.0), subjected to Ni<sup>2+</sup>-affinity purification and subsequent size exclusion chromatography. After purification, the sample was mixed with 10x molar excess of DTT and 5x molar excess of biliverdin, and left to incubate on ice in the dark overnight. Purified holoprotein was subjected to buffer exchange to get rid of excess biliverdin, concentrated to 20 mg/mL and flash frozen in liquid nitrogen.

**Mass Spectrometry.** The mass spectrometric experiments were performed with a QSTAR Elite ESI-Q-TOF mass spectrometer equipped with an API 200 TurboIonSpray

ESI source from AB Sciex (former MDS Sciex) in Concord, Ontario (Canada). The samples were injected into the ESI source with a flow rate of 15  $\mu\text{L}/\text{min}$ . The parameters were optimized for maximum abundance of the ions under study. Room-temperature nitrogen was used as nebulization (35 psi) and as curtain gas (18 psi). The ion-source voltages of 5.0 kV for capillary, 50 V for the orifice plate (declustering potential), 5 V as potential difference between skimmer and pre-quadrupole, and 200 V for the potential difference between the focusing ring and pre-quadrupole were used. Accumulation delay of 2 s, ion release delay of 6 ms and ion release width of 5 ms were used. Each spectrum was an average of spectra collected within 5 min, each of these containing 20 individual scans that were averaged before being sent from the instrument to the data system. The measurement and data handling was accomplished with Analyst® QS 2.0 Software. Mass spectra were externally calibrated by using ESI Tuning Mix (Agilent). MS experiments in denaturing conditions were measured of 3  $\mu\text{M}$  samples in MeOH/H<sub>2</sub>O/HAc (50/47/3 v/v %).

The molecular mass (most abundant) was calculated from the average of 10 most intense charge states. A deconvoluted molecular mass of 56.95 kDa was found for the unlabeled PAS-GAF-PHY construct, which corresponds well with the theoretical value of 56.97 kDa. The <sup>13</sup>C<sup>15</sup>N-labeled PAS-GAF-PHY resulted in a mass increment of 3169 Da. According to sequence (C<sub>2523</sub>H<sub>3943</sub>N<sub>713</sub>O<sub>736</sub>S<sub>15</sub>), the maximum number of <sup>13</sup>C isotopes is 2523 and of <sup>15</sup>N isotopes is 713. Considering mass increments of 1.003355 for <sup>13</sup>C and 0.997035 for <sup>15</sup>N, the maximum mass increment of PAS-GAF-PHY is 3242 Da, resulting in 97.7% labeling.

## Sample Preparation and Experiments

**Sample Preparation for FTIR Experiments.** 1.6 to 1.8  $\mu\text{L}$  of PAS-GAF-PHY were applied to a BaF<sub>2</sub> window (20 mm diameter). The sample was sealed without any drying between two windows using a small layer of vacuum grease (Glisseal). For <sup>13</sup>C<sub>4</sub>-Asp-labeled PAS-GAF-PHY, 3  $\mu\text{L}$  of sample were applied and slightly reduced in volume for one minute at ambient temperature and pressure. Infrared absorption spectra were recorded on a Bruker IFS 66/S spectrometer to control the preparation. The ratio of absorbance of the amide I / water band at 1650  $\text{cm}^{-1}$  to the amide II band at 1550  $\text{cm}^{-1}$  was between 2.9 and 2.2. This ratio indicates a full hydration of the sample.

**Time-Resolved Step-Scan FTIR Difference Spectroscopy.** Samples were maintained at 20 °C by a circulating water bath. Step-scan experiments were performed using a Bruker IFS 66v spectrometer with a photoconductive mercury cadmium telluride (MCT) detector at a spectral resolution of 8  $\text{cm}^{-1}$ . The spectral range was reduced to 1974 to 988  $\text{cm}^{-1}$  using a band-pass filter (Laser Components). The 10-ns actinic pulse with a wavelength of 660 nm and an intensity of about 4.5 mJ /  $\text{cm}^2$  was generated by a tunable optical parametric oscillator (Opta) pumped by the 355-nm third harmonic of a Nd:YAG laser (Quanta-Ray, Spectra Physics). The repetition rate was limited to 2 Hz by a shutter (LSTXY, nm Laser Products). After

each recording, the back reaction and full recovery of the Pr state of the sample was accelerated by exposure to a 40-ms pulse with a wavelength of 751 nm and an intensity of about 500 mW / cm<sup>2</sup> generated by a cw diode laser (Leading Tech Laser Company) and a shutter (UniBlitz) (hence, two-color step scan FTIR). The beam size of both beams was about 1 cm<sup>2</sup> at the sample. All components were synchronized by a pulse generator (DG645, Stanford Research Systems). Before the start of the step-scan experiment, each sample was adapted to the procedure by at least 10 sequences of exposure to a single laser pulse at 660 nm and six laser pulses at 751 nm. Then, the IR intensity was continuously monitored before and after excitation by 660 nm pulses in 1000 time slices of 5  $\mu$ s at 277 mirror positions with 8 coadditions each. FT was performed with a zero filling factor of 8. The resulting time resolution was 2.5  $\mu$ s and difference spectra were obtained up to 4.7 ms after excitation. Samples were used for up to four experiments corresponding to a maximum of 9000 excitations in total. 13 and 15 experiments were averaged for dimeric and monomeric PAS-GAF-PHY, respectively. For the <sup>13</sup>C<sup>15</sup>N-labeled and <sup>13</sup>C<sub>4</sub>-Asp-labeled samples, 18 and 21 experiments were averaged, respectively. In D<sub>2</sub>O, four experiments were averaged for each sample.

**Steady-State FTIR Difference Spectroscopy Using Laser Pulses.** FTIR difference spectra were generated using the setup for time-resolved experiments described above but with a resolution of 2 cm<sup>-1</sup>. 1024 scans were recorded before and after excitation with the 660-nm laser pulse generating a Pfr *minus* Pr difference spectrum. Afterwards, 1024 scans were recorded before and after excitation with the 751-nm laser pulse generating a Pr *minus* Pfr difference spectrum. A final exposure to five additional 751-nm pulses completed the recording. 6-12 difference spectra were averaged.

**Flash Photolysis.** The experimental details of the flash photolysis experiments are described in<sup>4</sup>. The excitation pulses at 700 nm (1.2 mJ/cm<sup>2</sup>, duration of 10 ns, and repetition rate 0.25 Hz) were generated by a tunable Ti:sapphire laser (Solar TII CF125 with built-in second harmonic generation), pumped by the second harmonic of a Nd:YAG laser (Solar TII LF-117). The continuous wave probe light was generated by a tungsten halogen lamp (AvaLight-HAL, Avantes). The time-resolved absorbance changes were monitored separately at 10 selected wavelengths ranging from 610 to 810 nm, in a random order to avoid systematic error. To improve the signal-to-noise ratio, interference filters (bandpass,  $\pm$ 15 nm) were inserted before and after the sample position and 100 measurements were averaged at each wavelength. The optical response was recorded with a photomultiplier tube (Hamamatsu) and digitized in an oscilloscope (300 MHz; Tektronix). The sample sat in a vertically mounted glass capillary with an inner diameter close to 1.1 mm (VITREX) with an absorbance at 700 nm of about 0.2 to 0.4/mm. To avoid excessive sample degradation, the sample solution (volume 400  $\mu$ L) was cycled using a peristaltic pump (Ismatec, Reglo Digital) at a flow rate of 0.5 mL/min through a glass reservoir, the capillary, and connecting Teflon tubing (1-mm inner diameter). A far-red diode (751nm, 3mW; Leading-Tech Laser Co.) was used to revert the sample to the Pr state by constant illumination through the Teflon tubing.

**Data Analysis.** The data-sets were averaged on a logarithmic time scale and analyzed using MATLAB (The Mathworks). Each spectrum was corrected for water contributions at around 1650  $\text{cm}^{-1}$  with a set of experimentally determined water difference spectra as described previously<sup>5</sup> and baseline-corrected manually to obtain the data matrix **A**. On this matrix, a weighted global fit was performed with weighting factors calculated from the variance of the absorbance at the different wavenumbers determined from the reference intensity<sup>5</sup>. A model of sequential reactions with three intermediates was postulated and yielded better agreement to the data than using fewer or more intermediates. The species-associated difference spectra (SADS) **D** were calculated using the concentration profiles **C** from the global fit via matrix division according to  $\mathbf{D}=\mathbf{AC}^+$  (with  $\mathbf{C}^+$  being the pseudoinverse of **C**).

The global fit of the  $^{13}\text{C}^{15}\text{N}$ -labeled sample yielded time constants of 93  $\mu\text{s}$ , 1.03 ms and >5 ms for Lumi-R, Meta-R and Pfr, respectively. These time constants are similar to those of the unlabeled sample. The global fit of the  $^{13}\text{C}^{15}\text{N}$ -labeled sample in  $\text{D}_2\text{O}$  was performed in the spectral range of 1699-1800  $\text{cm}^{-1}$  and yielded time constants of 130  $\mu\text{s}$ , 1.67 ms and >4 ms for Lumi-R, Meta-R and Pfr, respectively.

For the experiments in  $\text{D}_2\text{O}$ , spectra representing Lumi-R in  $\text{D}_2\text{O}$  were averaged in the time range 2.5-12.5  $\mu\text{s}$ . Spectra representing Meta-R were selected by the presence of the characteristic band at 1725 (+)  $\text{cm}^{-1}$ , and averaged in the time ranges 275-548  $\mu\text{s}$  and 218-435  $\mu\text{s}$  for unlabeled and  $^{13}\text{C}^{15}\text{N}$  labeled samples, respectively. Spectra representing Pfr in  $\text{D}_2\text{O}$  were recorded at 4.35 ms.

**Femtosecond Pump-Probe IR Spectroscopy.** The samples were measured at a room temperature of 21°C in buffered  $\text{D}_2\text{O}$ . The pH of 30 mM Tris in  $\text{D}_2\text{O}$  was adjusted with concentrated HCl in  $\text{H}_2\text{O}$  to pH 8 measured with a standard glass electrode which corresponds to pD 8.4<sup>6</sup>. The buffer of the samples was exchanged by repeated dilution and concentration with Amicon Ultra 10 K centrifugal filters.

In buffering to  $\text{D}_2\text{O}$ , the protein was switched between Pr and Pfr by illumination with laser diodes at 655 nm and 780 nm in 5 min intervals for 1 hour. The sample was circulated in a closed-cycle flow-cell with  $\text{CaF}_2$  windows with 50  $\mu\text{m}$  pathlength<sup>7</sup> with an OD of 0.2 at the excitation wavelength and 0.5 at 1640  $\text{cm}^{-1}$ , which corresponds to about 0.02 at 1700  $\text{cm}^{-1}$ . The flow rate was adjusted to ensure complete sample exchange at a 1 kHz repetition rate. The flow cell system contained a sample reservoir, which was continuously illuminated with an LED at 780 nm (10 mW), in order to keep the protein in the Pr state. Additionally, only dim light was used in the laboratory and accessible parts of the flow cell system were covered.

The UV/vis pump-mid-IR probe setup has been described earlier<sup>8</sup>. In short, a 1 kHz Ti:sapphire laser (Quantronix) was used to generate visible pump pulses by a TOPAS (traveling-wave optical parametric amplifier of superfluorescence, LightConversion Inc.) and mid-IR pulses by an optical parametric amplifier<sup>9</sup>. The time delay between the two beams was varied by a delay stage. The IR beam was separated into a probe and reference beam. A synchronized chopper blocked every second visible pump pulse (692 nm, 500 nJ, 300  $\mu\text{m}$  diameter) overlapped with the probe beam (150  $\mu\text{m}$

diameter). The transient signal was obtained by comparing probe and reference signals with and without visible excitation.

The IR beams were dispersed in a spectrograph and detected with a  $2 \times 64$  channel double array HgCdTe detector (Infrared Systems Development). A spectral window was between  $80\text{ cm}^{-1}$  and  $100\text{ cm}^{-1}$ . Several overlapping spectral positions of the spectrograph was used to capture the range of  $1800\text{ cm}^{-1}$  to  $1500\text{ cm}^{-1}$ . Waterlines were used for spectral position calibration. The spectral resolution was  $2\text{ cm}^{-1}$ , determined by the FWHM of the waterlines. A more detailed description of this setup is described elsewhere.<sup>8</sup>

For averaging the Lumi-R spectrum, 30 different time points between 2.6 ns and 2.66 ns after excitation were summed up for at least 10 scans with 500 shots for each spectral position. The transient spectra from 1 ps to 2.6 ns for the unlabeled sample are presented in Lenngren et al.<sup>10</sup>

## Molecular Dynamics Simulations

Three systems were simulated using the molecular dynamics (MD) simulation package GROMACS<sup>11–14</sup>. These included: Pr, Pr with isomerized biliverdin chromophore, and Pfr. The starting structures were taken from the PDB coordinate files, 4Q0J<sup>15</sup> (Pr) and 5C5K<sup>16</sup> (Pfr). The missing residues were modelled using MODELLER<sup>17,18</sup>. The protonation states of all histidines were modelled as neutral, with a proton on the Ne. The protein was described using the AMBER03 forcefield<sup>19</sup>, and the water molecules using the TIP3P model<sup>20</sup>. The partial charges of biliverdin atoms and of the atoms of the cysteine bound to biliverdin (Cys 24) are derived using the Restricted Electrostatics Potential (RESP)<sup>21</sup> procedure (Table S1 and Table S2). The other force field parameters are assigned based on the similarity to atoms already defined in the force field (Table S1 and Table S2).

During the MD simulation, interactions between atoms within 1 nm are evaluated at each step, while beyond 1 nm interactions are evaluated each tenth step. Periodic boundary conditions were applied. The Particle-Mesh-Ewald (PME)<sup>22,23</sup> is used for long-range electrostatics interactions, with a grid spacing of 0.12 nm and an interpolation order of 4. The Lennard-Jones long-range cut-off is set to 1 nanometer. Beyond this cutoff, a dispersion correction is applied for the energy. Constant pressure and temperature are maintained by weakly coupling the system to an external bath at 1 bar pressure and 300 K, using the Berendsen barostat<sup>24</sup> and the V-rescale thermostat<sup>25</sup> with coupling times of 1.0 and 0.1 ps, respectively. A leapfrog integrator is used with an integration time step of 2 fs. Bond distances and bond angles of water molecules are constrained using SETTLE<sup>26</sup>. Other bond distances are constrained using LINCS<sup>27</sup>.

Each structure was minimized using 200 steps of steepest descent approach, and it was placed in a dodecahedron box, which was subsequently filled with 46058 (Pr) and 46380 (Pfr) water molecules. Sodium and chloride ions were added up to a concentration of approximately 0.15 M, and in such a way that the total charge of the

system was neutral. The total number of atoms was 154266 and 154918, for the Pr and Pfr systems, respectively. Water molecules and protein atoms missing in the PDB coordinate file were equilibrated during 10 ns of MD with position restraints (force constant 1000 kJ mol<sup>-1</sup> nm<sup>-2</sup>) on the remaining heavy atoms. Each system (Pr, Pfr) was then simulated for 700 ns, of which the last 500 ns were used for data collection.

The chromophore of the Pr conformation was isomerized using force probe simulations, in which the minimum of the dihedral angle C4C-CHD-C1D-ND (Figure S8) was shifted from 0 to 180 degrees during 100 picoseconds using the free energy perturbation method<sup>28</sup> in GROMACS<sup>11-14</sup>, similarly to Andresen *et al.*<sup>29</sup> At the same time the atomic charges of the chromophore and of Cys 24 were changed from Pr to Pfr (Table S1 and Table S2). The 1-4 bonded interaction between C4C and ND was excluded. The dihedral angle was described using a periodic function with force constant 100 kJ/mol and multiplicity 1. For the force constant, a value of 100 kJ/mol assured that most of the force probe simulations reached the final isomerized state within 100 ps of simulation. A similar value of force constant has been used previously in a related application.<sup>29</sup> A multiplicity of one was chosen to avoid that other minima could be occupied during the perturbation. We note that this description of the torsion was only used during the force probe simulations.

Force probe simulations were started from 100 frames collected from the simulation of the Pr state (every nanosecond during time 400 to 500 nanoseconds). The minimum of the C4C-CHD-C1D-ND dihedral angle was shifted in both directions, modelling rotation of the D-ring in a clockwise and counter-clockwise direction, for a total of 200 force probe simulations (Figure S8). Both monomers were isomerized. To model isomerization of the phytochrome chromophore, the direction of rotation was chosen clockwise (Figure S8a,b), as rotation in this direction produced structures which resembled more closely the crystal structures of the Pfr phytochrome chromophore (5C5K,<sup>16</sup> 4O01<sup>30</sup>) (Figure S8c). The clockwise direction of rotation for the biliverdin chromophore is in agreement with previous data and calculations.<sup>31</sup> A subset of the structures obtained from the clockwise force probe simulations were selected and used as starting structures for standard MD simulations (described above) of the Lumi-R state. In particular, we performed four longer simulations (2x1000ns and 2x500 ns) and ten shorter simulations (10x50 ns). The C4C-CHD-C1D-ND dihedral angles of the starting structures of the four longer simulations are (in degrees) for monomers A and B, respectively: -158.7 and -166.5; -163.8 and -160.7; -163.9 and -164.9; -160.7 and -167.1. The four longer simulations (in total 3000 ns) served to obtain the average structure of Lumi-R as described in a separate section of the SI Methods.

Figure S13 shows that the distributions of a set of selected distances in the chromophore binding pocket are comparable between the MD simulations of Lumi-R, even though differences in the occupancies are observed. An exception is monomer B of the second 1000 ns simulation (run 2) where Tyr 176 and Arg 466 show increased flexibility. We also notice that the distance between the D-ring O and Tyr 176 converges more slowly, as only in one fourth of the shorter 50 ns simulations it

reaches the value observed in the longer ones. Figure S9 shows how these distances evolve as a function of time for the four longer simulations.

The root mean square deviation (RMSD) of each monomer of the phytochrome phytochrome in the Pr, Pfr and Lumi-R states MD simulations is shown in Figure S10, indicating an overall stable backbone conformation. Coordinates were recorded every 10 picoseconds. Images and movie were edited using the PyMOL and VMD<sup>32</sup> molecular visualization programs.

**Computation of the average structures from the trajectories.** We produced average structures for Pr, Pfr, and Lumi-R from the respective trajectories by aligning the structures on the rings A-C of the biliverdin. Then we computed the electron density of each frame using *sfall* of the *ccp4* package. The density was then computed for the protein and waters separately, in a box of dimensions 40x40x79Å, up to 1Å resolution and for space group P1. The densities were averaged using a Matlab code. The residues shown and labeled in Figure 4 were placed in these densities using real space refinement in *coot*. The four long Lumi-R trajectories were averaged together for the representation in Figure 4. When inspecting the densities computed for individual Lumi-R runs we observed that while R466 was always in hydrogen bonding distance to the D-ring C=O, the position of the D207 side chain varied such that that it could form either one or two bonds to R466. Also, the mobile water had different occupancies as shown in Figure 4d.

## Comparison of the Hydrogen Bond Strength from Experiments and Simulations

It is interesting to compare the hydrogen bonding strength in the trajectories of the Pr, Pfr and Lumi-R states to the corresponding infrared spectra. Fried and Boxer have suggested that computation of the difference in electric field ( $|\vec{F}_{vib}|$ ) acting on the C and O atoms of the carbonyl probe correlates with the spectral position.<sup>33</sup> We computed  $|\vec{F}_{vib}|$  from the MD trajectories, and found that the peaks of the distributions (Figure S12) correlate well with the spectral positions for Pr and Lumi-R, but not in Pfr. This disagreement of the model with the observations could be because a possible covalent character of hydrogen bonds<sup>34</sup> is neglected in the electrostatic model. The D-ring C=O may experience a very tight hydrogen bond with the side chain of His201, which has a very short distance in one of the monomers in the crystal structure. We stress that the strong downshift of the C=O absorption in Pfr may be caused by other effects and not only hydrogen bonding, for example a change in the aromatic character in the chromophore. It should be noted that the C=O peak in the Pfr state of the *D. radiodurans* phytochrome appears at unusually low wavenumbers compared to other phytochromes.<sup>35</sup> We note that the trajectories of Pr and Pfr are in excellent agreement with the crystal structures.<sup>16,30</sup> Both are very stable structures as judged by the average electron densities and RMSDs of the backbone carbons in Figures 4 and S10. Furthermore, the *distribution* of hydrogen bond strength is well reproduced by the model for all three states, indicating a broad



distribution in Lumi-R and narrower distributions in Pr and Pfr (Figure S12). This is in agreement with the experimental data as described in the main text.

## Supplementary Figures

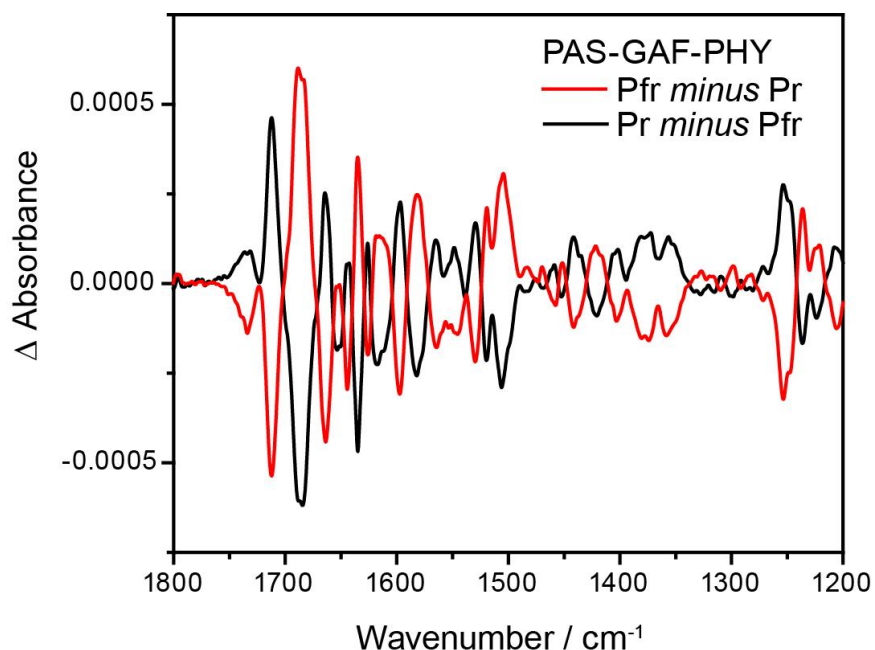


**Figure S1.** Full recovery of the Pr state as demonstrated by steady-state FTIR difference spectra generated by single laser pulses of red and far-red light. The light-induced difference spectra of PAS-GAF-PHY dimer were generated under the same conditions as the time-resolved spectroscopy. After taking a reference spectrum, the conversion of Pr to Pfr was induced by a single 10 ns laser pulse at 660 nm generating a Pfr *minus* Pr difference spectrum (red). Subsequently, another reference spectrum was recorded and the sample was excited by a single 40-ms laser pulse at 751 nm, which generated a Pr *minus* Pfr difference spectrum (black). A complete mirror image is obtained, which demonstrates that the sample fully recovered to Pr after this procedure. Such full reversibility is mandatory for performing step-scan experiments.

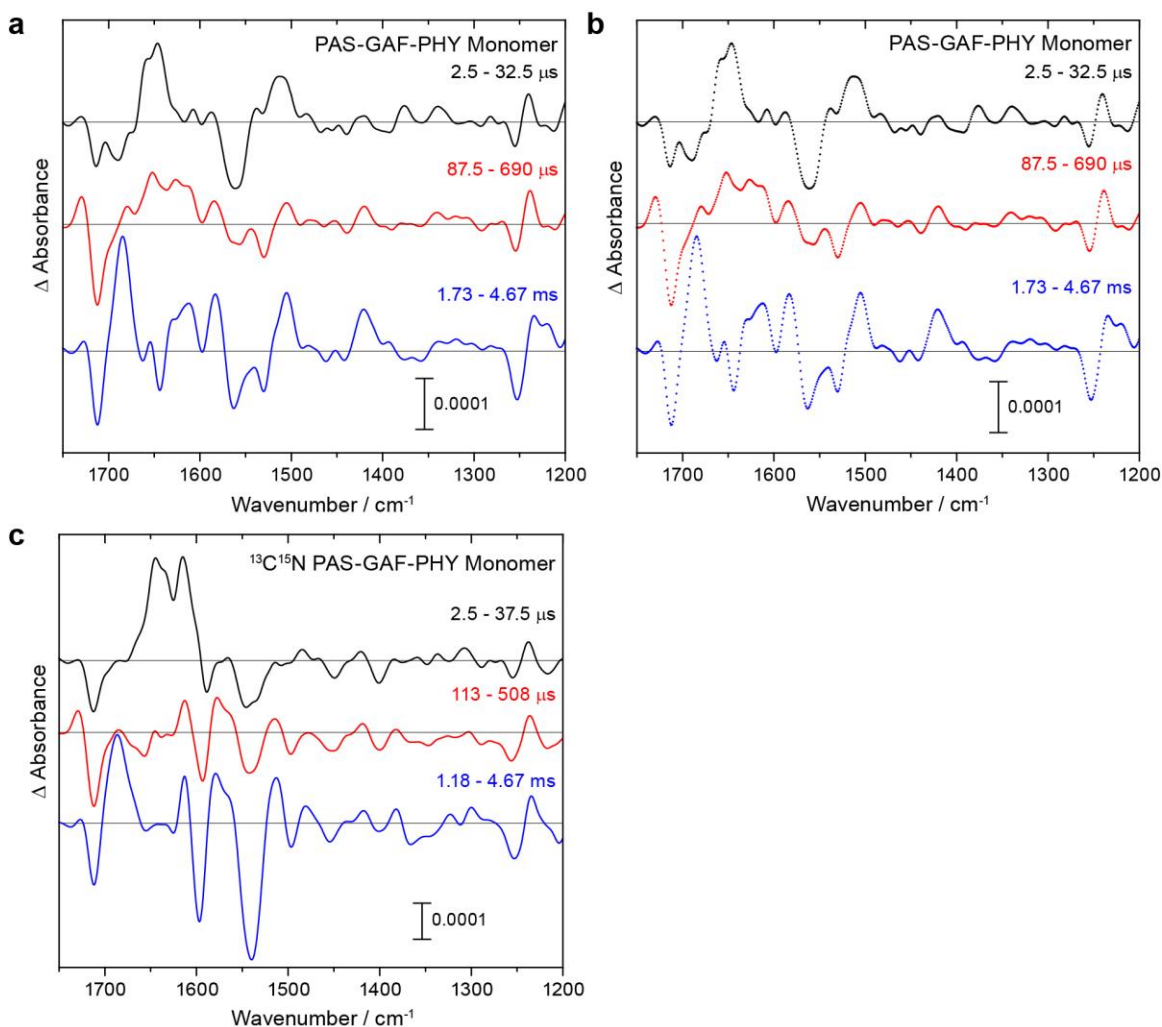


**Figure S2.** Raw data from time-resolved FTIR spectroscopy. The spectra were averaged over time windows according to the maximal concentrations of the species from the global fit (cutoff at 65%). (a) Three characteristic spectra are obtained from averaging raw data of the photoreaction of the PAS-GAF-PHY monomer. (b) The spectra of the PAS-GAF-PHY monomer are shown as scatter plots instead of line graphs to illustrate the close spacing of data points despite the low spectral resolution of 8  $\text{cm}^{-1}$ , which is achieved by a zero filling factor of 8 before Fourier transformation. (c) The spectra for the  $^{13}\text{C}^{15}\text{N}$  labeled PAS-GAF-PHY are averaged over slightly different time windows in agreement with the rate constants obtained from the global fit.

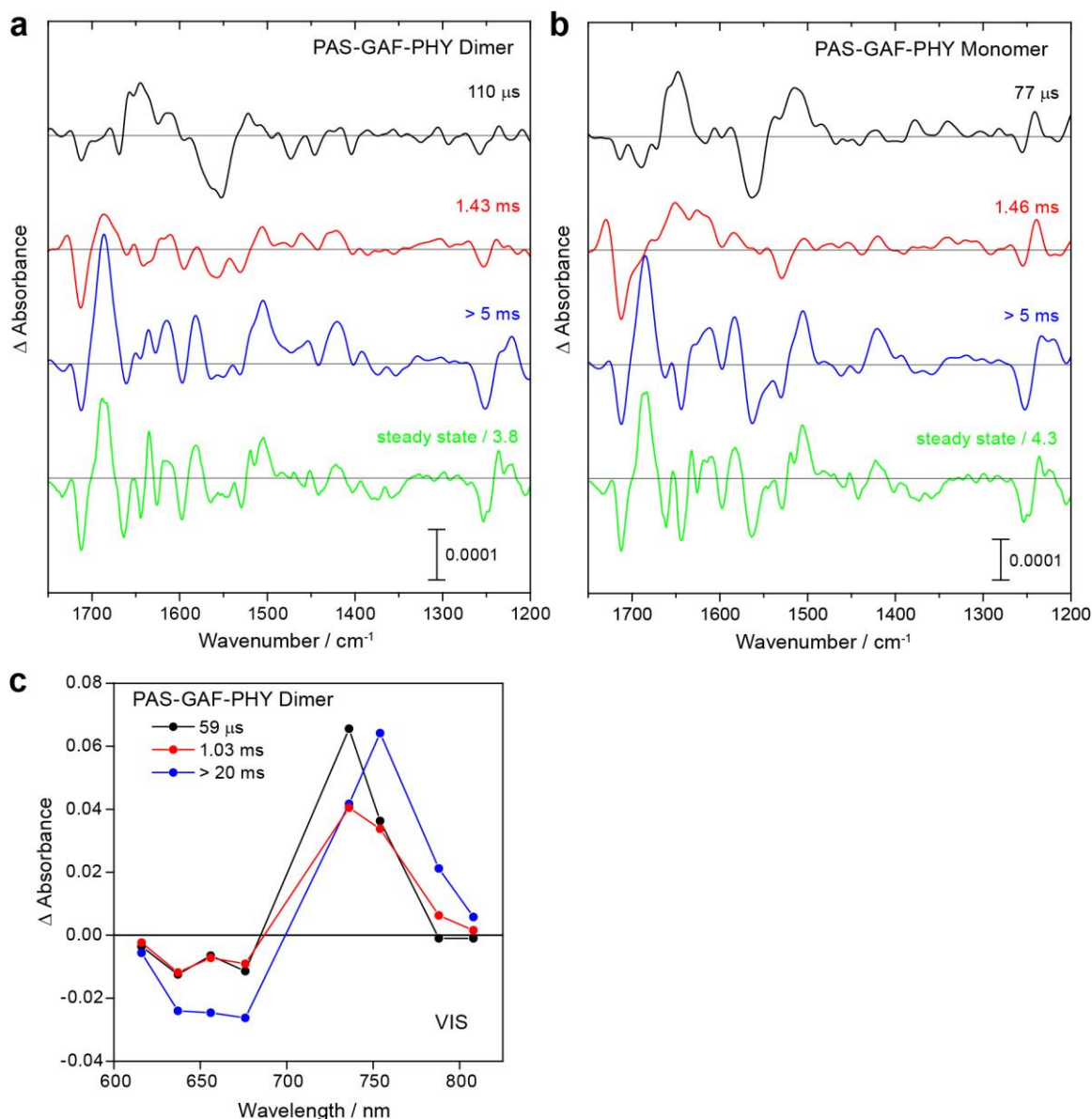


**Figure S3.** Time-resolved FTIR and visible spectroscopy on dimeric *DrBphP*<sub>PSM</sub>. (a) The transient spectra were analyzed by global fitting and the resulting three SADS are depicted with the respective time constants. For comparison, the steady-state spectrum of the Pr to Pfr conversion is included at the bottom. (b) The SADS and time constants of the monomeric variant are in general agreement with those of the dimer. (c) The SADS from analysis of flash photolysis experiments in the visible spectral region show the typical photo-induced shift from red to far-red absorption of Lumi-R, Meta-R and Pfr<sup>4</sup>.

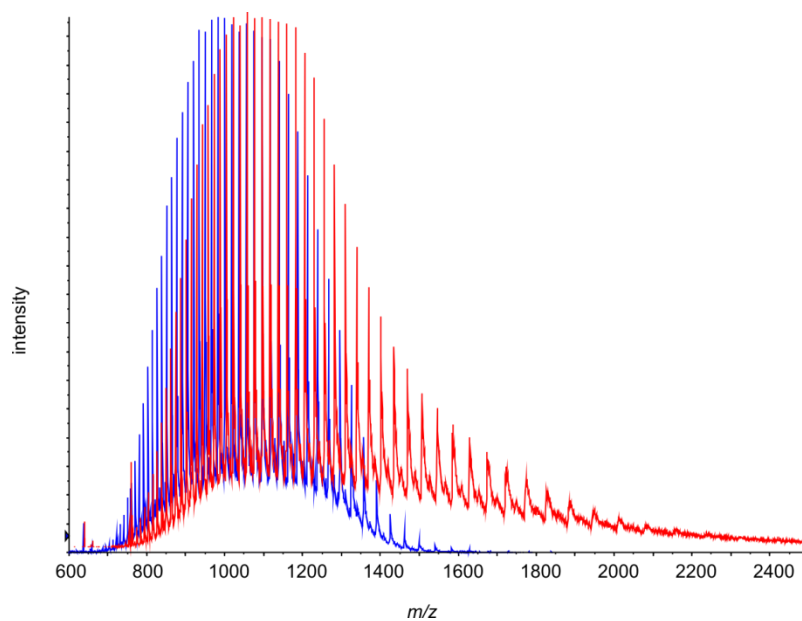


**Figure S4.** Mass spectrometry data of the *DrBphPPSM*. ESI-MS spectra of unlabeled (blue) and  $^{13}\text{C},^{15}\text{N}$ -labeled (red) PAS-GAF-PHY in MeOH/H<sub>2</sub>O/HAc (50:47:3). The data confirms that more than 97 % of the C and N atoms are labeled.

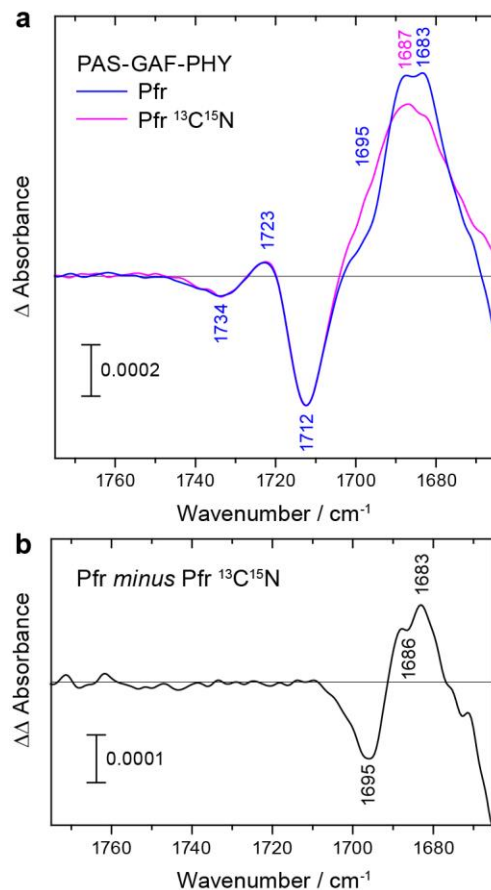


**Figure S5.** Difference spectra of Pfr *minus* Pr from steady-state FTIR spectroscopy. (a) The comparison of the unlabeled PAS-GAF-PHY monomer with the <sup>13</sup>C<sup>15</sup>N-labeled sample shows a negative contribution at ~1695 cm<sup>-1</sup> in the spectrum of the unlabeled sample, which is downshifted out of the presented spectral window upon labeling. This observation supports the presence of a similar difference in the time-resolved spectra of Pfr shown in Figure 3d at lower spectral resolution. Each spectrum was generated by a single laser excitation. (b) The double difference of the spectra resolves an additional negative indentation at 1686 cm<sup>-1</sup>, which is similar in frequency to the negative signal detected for the Lumi-R intermediate as shown in Figure 3g.

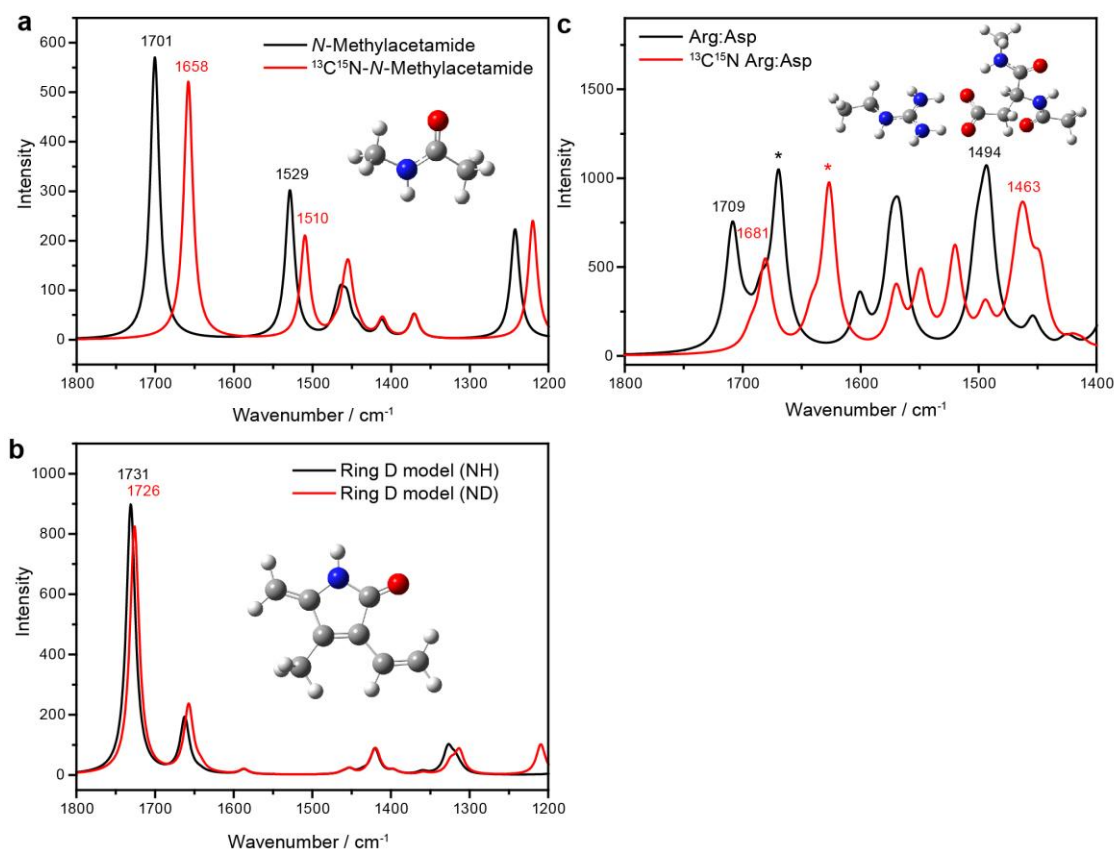


**Figure S6.** Quantum chemical calculations on the downshift of the amide modes by  $^{13}\text{C}^{15}\text{N}$  labeling, of the carbonyl mode of ring D by deuteration, and of the arginine and aspartate modes by  $^{13}\text{C}^{15}\text{N}$  labeling. (a)  $^{13}\text{C}^{15}\text{N}$  labeling induces a downshift in frequency of the amide I mode by  $43\text{ cm}^{-1}$  and of the amide II mode by  $19\text{ cm}^{-1}$  in the model compound *N*-methylacetamide. Transition dipole coupling of amide modes has been neglected for simplicity. Similar downshifts of  $41\text{ cm}^{-1}$  and  $27\text{ cm}^{-1}$ , respectively, were obtained when an explicit solvation was included by 3  $\text{H}_2\text{O}$ . Similar values have been detected experimentally.<sup>36</sup> (b) Deuteration of NH induces a downshift in frequency of the carbonyl mode of dihydro-pyrrol-2-one by  $5\text{ cm}^{-1}$ . The structure of the compound was selected as a model for the ring D pyrrole of biliverdin (see inset). (c)  $^{13}\text{C}^{15}\text{N}$  labeling induces a downshift of the high-energy arginine (CN) stretch by  $\sim 30\text{ cm}^{-1}$ . The asymmetric ( $\text{COO}^-$ ) stretch of aspartate is calculated to shift to below  $1500\text{ cm}^{-1}$  by forming a salt bridge with arginine. The model compound used for the calculations is shown in the inset. The asterisks indicate contributions from amide I modes of the backbone. The geometries were optimized and frequencies of normal modes were calculated using density functional theory (B3LYP, 6-311+G(2d,p)) implemented in *Gaussian03W*.<sup>37</sup> A single scaling factor of 0.98 was applied to the frequencies. The line spectrum was broadened for representation with Lorentzians (half maximum of  $14\text{ cm}^{-1}$ ).

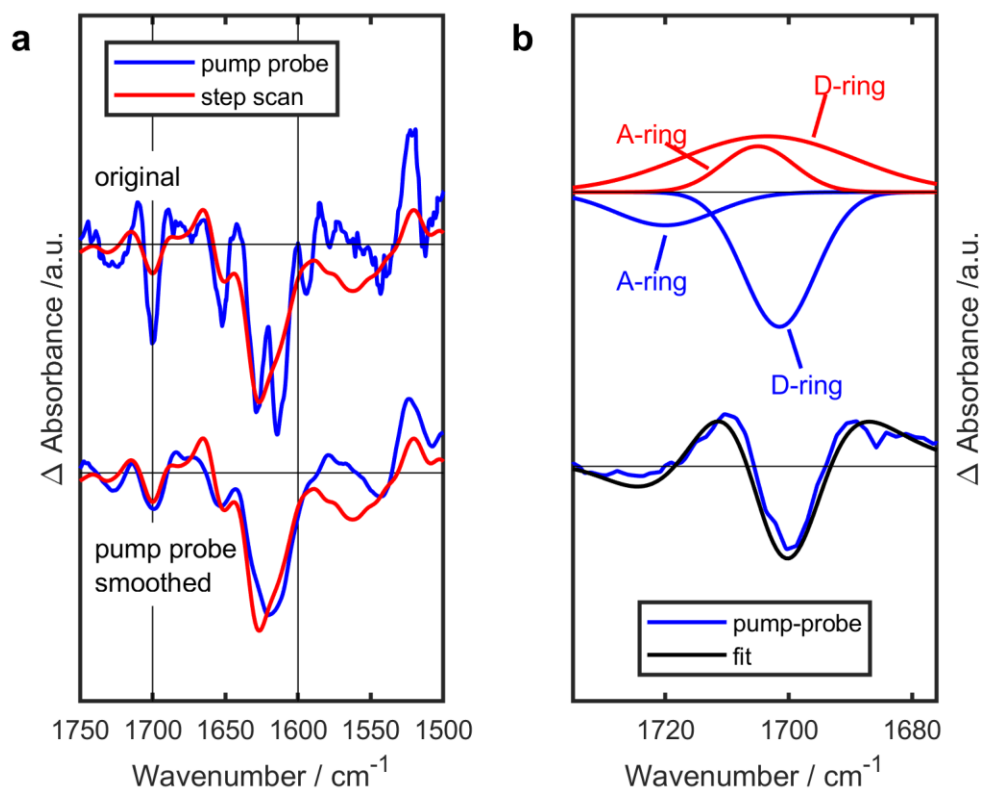


**Figure S7.** Comparison between the Lumi-R spectrum in D<sub>2</sub>O recorded by step-scan and by pump-probe infrared spectroscopy and Gaussian fit of the carbonyl region. (a) The upper set of difference infrared spectra is for the PAS-GAF-PHY construct from *D. radiodurans*. The Lumi-R SADS as recorded by step-scan compared to the pump-probe spectrum at 2.6 ns delay time (same spectrum as in Figure 3h). In the lower set of spectra, the same spectra are shown, but the pump-probe spectrum was filtered with a 13 point running average filter, which corresponds to lowering the spectral resolution of the pump-probe spectrum (2 cm<sup>-1</sup>) to better match the resolution of the step-scan experiment (8 cm<sup>-1</sup>). The pump-probe spectrum was corrected for baseline artefacts by adding a constant offset of 0.01 mOD. This offset corresponds to approximately 20% of the peak intensity at 1700 cm<sup>-1</sup>. The drift in baseline probably arises from the fact that the pump-probe acquisition is prone to errors in baseline when recording small signals (-0.05 mOD at 1700cm<sup>-1</sup>). The step-scan and pump-probe data was recorded on monomeric and dimeric samples, respectively. (b) The pump-probe spectrum at 2.6 ns is compared to a fit (lower set of spectra) consisting of four Gaussian peaks, which are a positive (representing Lumi-R) and negative (representing Pr) peak each for the A- and D-ring carbonyl (upper set of spectra). The Gaussian peak was computed as  $I = \frac{1}{\sigma_c \sqrt{2\pi}} \exp\left(-\frac{(\mu - \mu_c)^2}{2\sigma_c^2}\right)$ , with  $I$  as the spectral intensity,  $\mu$  as frequency,  $\sigma$  as the spectral width, and  $\mu_c$  as the frequency of the peak  $c$ . A residual was not minimized, but the peak positions were adjusted manually to match the spectrum. The width of the peaks was chosen to be 7 cm<sup>-1</sup>, except for the



positive (Lumi-R) peak of the D-ring, which was set to 20 cm<sup>-1</sup>. The intensity of the peaks from the A-ring were scaled by a factor of 0.5 compared to the peaks of the D-ring.

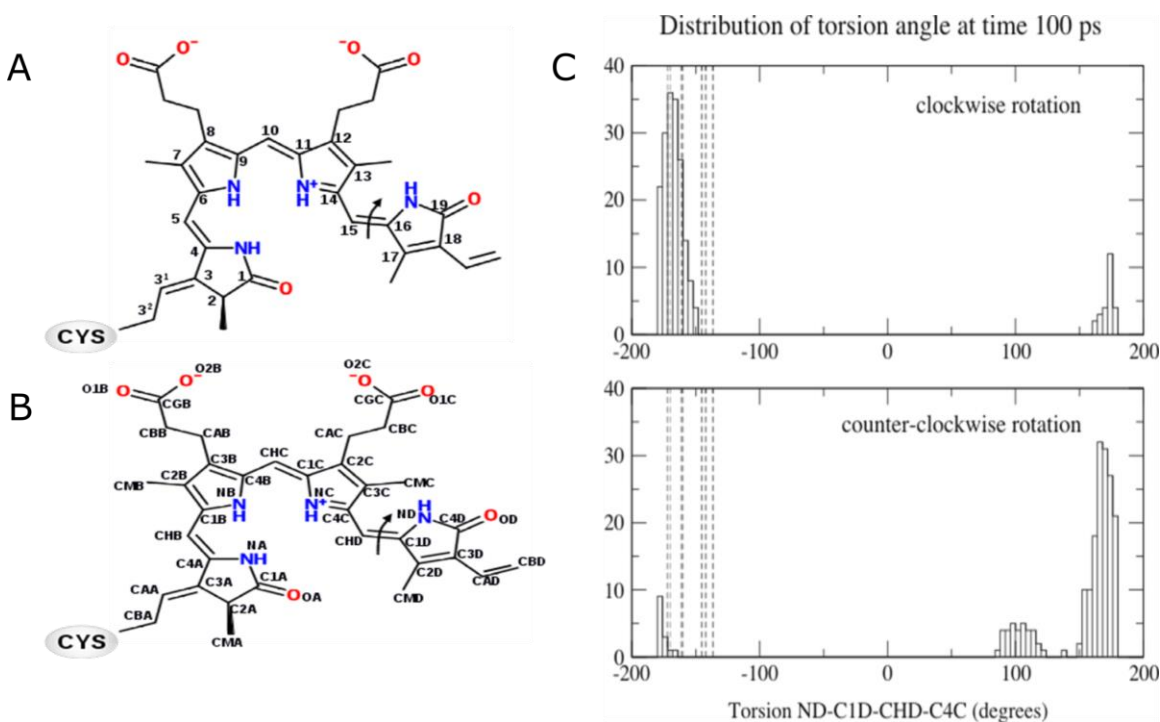


**Figure S8.** Biliverdin structure and distribution of torsion angles from the 100 ps force probe simulations. (a) and (b) Schematic representations of biliverdin (BV) in the Pr conformation. Biliverdin atom numbers (a) and names (b) as used in the text. Phytochrome isomerization was modeled by rotating the double bond between atoms 15 (CHD) and 16 (C1D). The clockwise direction of rotation is indicated by the black arrow. (c) Distribution of the ND-C1D-CHD-C4C torsion at the end (time step 100 ps) of 100 clockwise and 100 counter-clockwise force probe simulations of biliverdin isomerization around bond CHD-C1D of both monomers of the phytochrome. The dashed lines show the torsion angles observed in the crystal structures of the Pfr state of the phytochrome from *D. radiodurans* 5C5K (four monomers) and 400P (four monomers). The highest density is found around an angle of -168 degrees for the clockwise, and around an angle of +172 degrees for the counter-clockwise rotation.

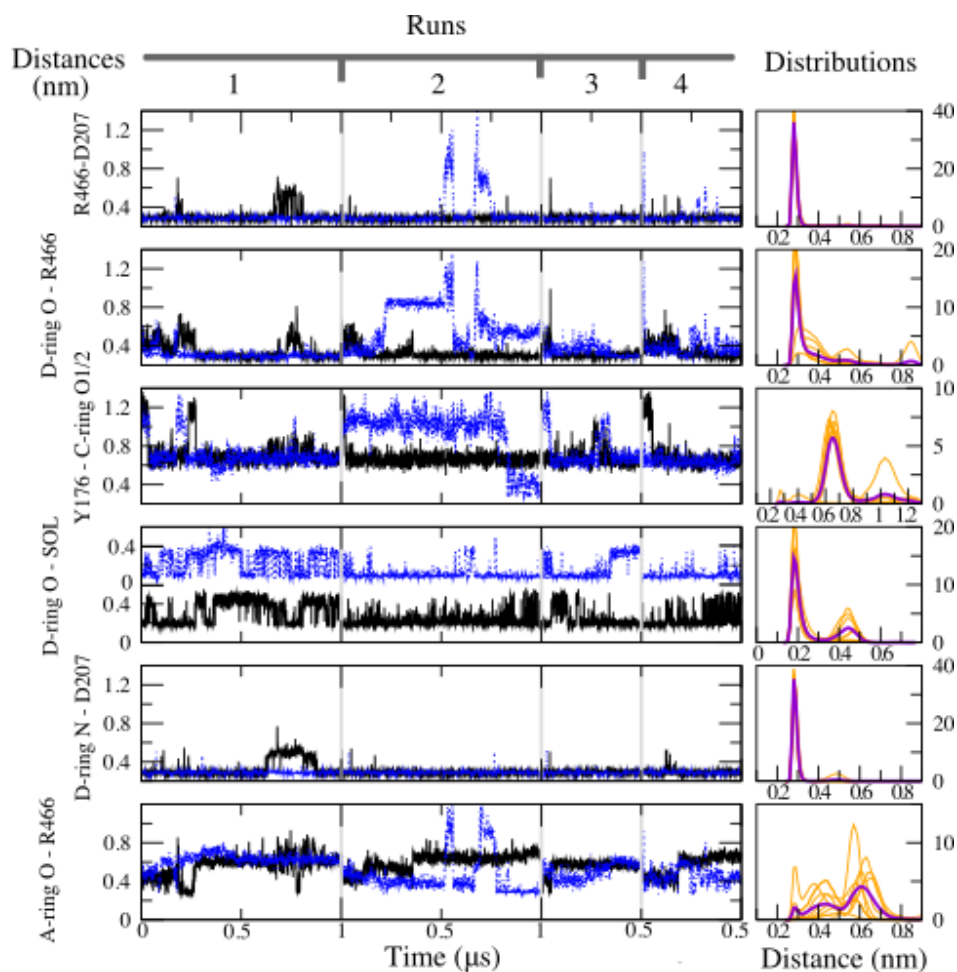


**Figure S9.** Inter-atomic distances and distributions in monomer A and monomer B during four molecular dynamics simulation of Lumi-R (runs 1-4: simulation lengths of 1, 1, 0.5 and 0.5 microseconds, respectively). *Left*, minimum distances as a function of time for monomers A (black) and B (blue); *right*, distributions of respective distances for each monomer of runs 1-4 (orange) and for all runs (violet). The distances are calculated as the minimum distances between R466 (atoms NH1 and NH2) and D207 (atoms OD1 and OD2), R466 (atoms NH1 and NH2) and biliverdin D-ring O, Y176 (atom OH) and C-ring (atoms O1 and O2, Figure S8), D-ring O and solvent atoms, D-ring N and D207 (atoms OD1 and OD2), and A-ring O and R466 (atoms NH1 and NH2).

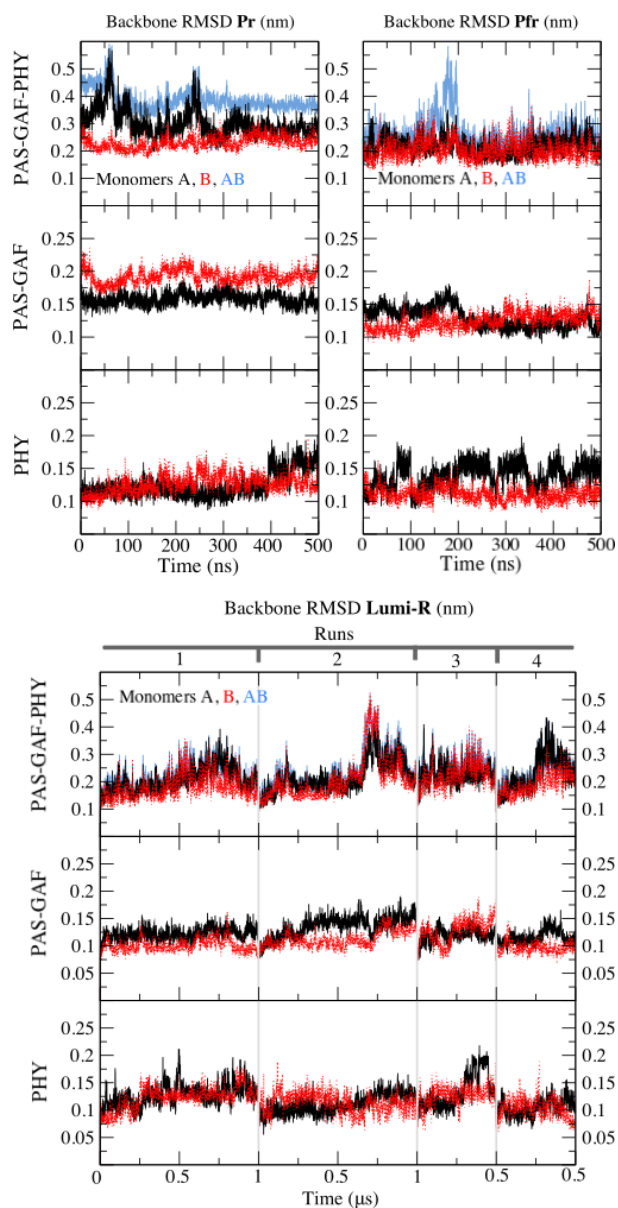


**Figure S10.** Root mean square deviation (RMSD) of the backbone atoms in Pr, Pfr, and Lumi-R simulations (runs 1-4: simulation lengths of 1, 1, 0.5 and 0.5 microseconds, respectively). For each simulation, RMSD of residues 20-500 (PAS-GAF-PHY), of residues 20-300 (PAS-GAF), and of residues 340-445, and 481-500 (PHY) is shown. RMSD of monomer A (black), monomer B (red), and monomers A and B together (cyan) are shown separately. RMSD is calculated from the starting structure (for Pr and Pfr the starting structures are taken at time 0 of the 200 ns equilibration runs, which are not shown in the figure).

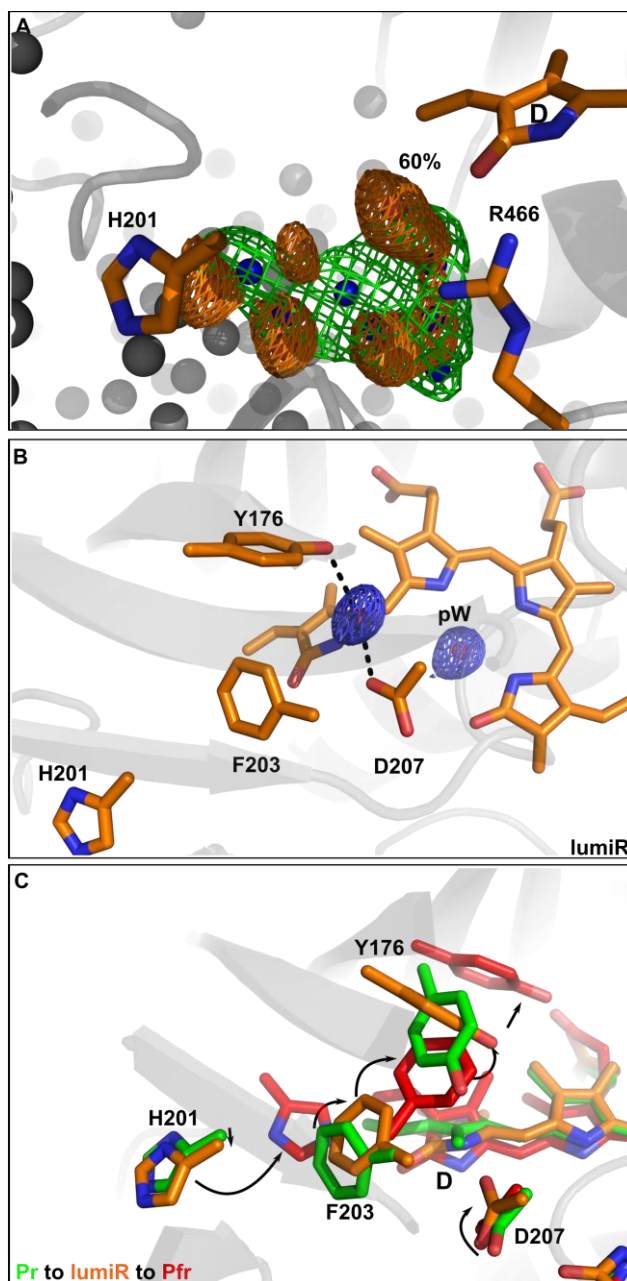


**Figure S11.** Details on the Lumi-R structure from molecular dynamics simulations. (a) The water channel to the bulk water (grey waters) is present in Pr (green mesh, blue waters) and Lumi-R (orange mesh, red waters). The electron densities were computed from the MD trajectories as described in SI Methods. (b) A connection between Y176 and D207 is established through a stable water in Lumi-R. (c) Rotation of the D-ring from Pr to Lumi-R and further to Pfr causes a rotation in residues Y176 and F203, and a movement of H201. The color coding of the structures is shown in panel c for all panels. The structures were refined against the average electron densities using real-space refinement in coot.

LumiRmonBphe470.mpg

**Movie S1.** The dynamics of the biliverdin, R466 (side chain atoms), F469 and F198 from the B monomer of the Lumi-R phytochrome during 1000 nanoseconds of molecular dynamics simulations. In the movie, F469 is on the left of F198. The water molecules within a distance of 0.35 nm from the D-ring O are shown. Snapshots are taken every nanosecond. The atoms' positions of protein and biliverdin are averaged every two frames. The movie demonstrates the highly dynamic environment of the D-ring C=O group in the Lumi-R state, both in terms of the R466 interaction to the biliverdin and the dynamic water molecules in the water trail next to the biliverdin molecule.

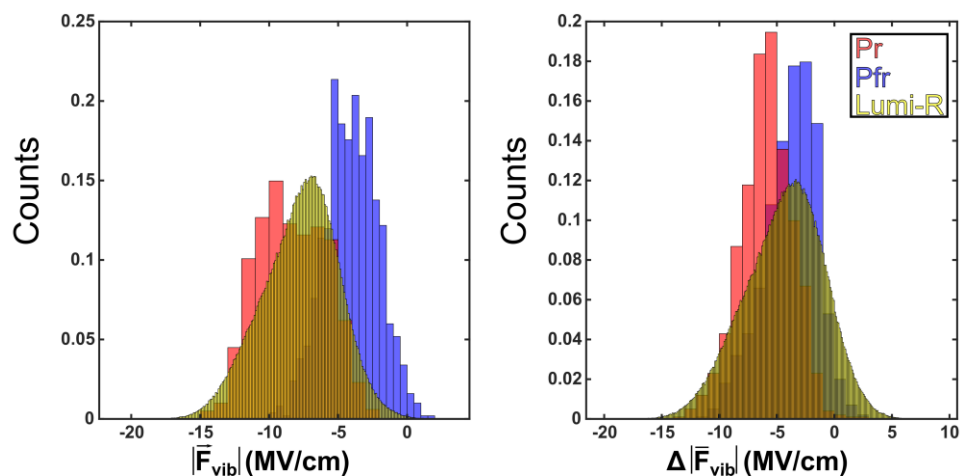


**Figure S12.** Electric field acting on the C=O (D-ring). The normalized electric field<sup>33</sup> ( $|\vec{F}_{vib}|$ ) and the electric field difference between the C and O atoms ( $|\Delta\vec{F}_{vib}|$ ) distributions as histograms. The Lumi-R (yellow) state was sampled every 10 ps along a total of 3000 ns molecular dynamics simulation (four trajectories, 2x1000 ns and 2x500 ns), while Pr (red) and Pfr (blue) were sampled every 1 ns along a 500 ns molecular dynamics simulation. The data show that the width of the distribution in Lumi-R is significantly larger compared to Pr and Pfr, supporting the broad spectral shape detected for the C=O peak in Lumi-R.

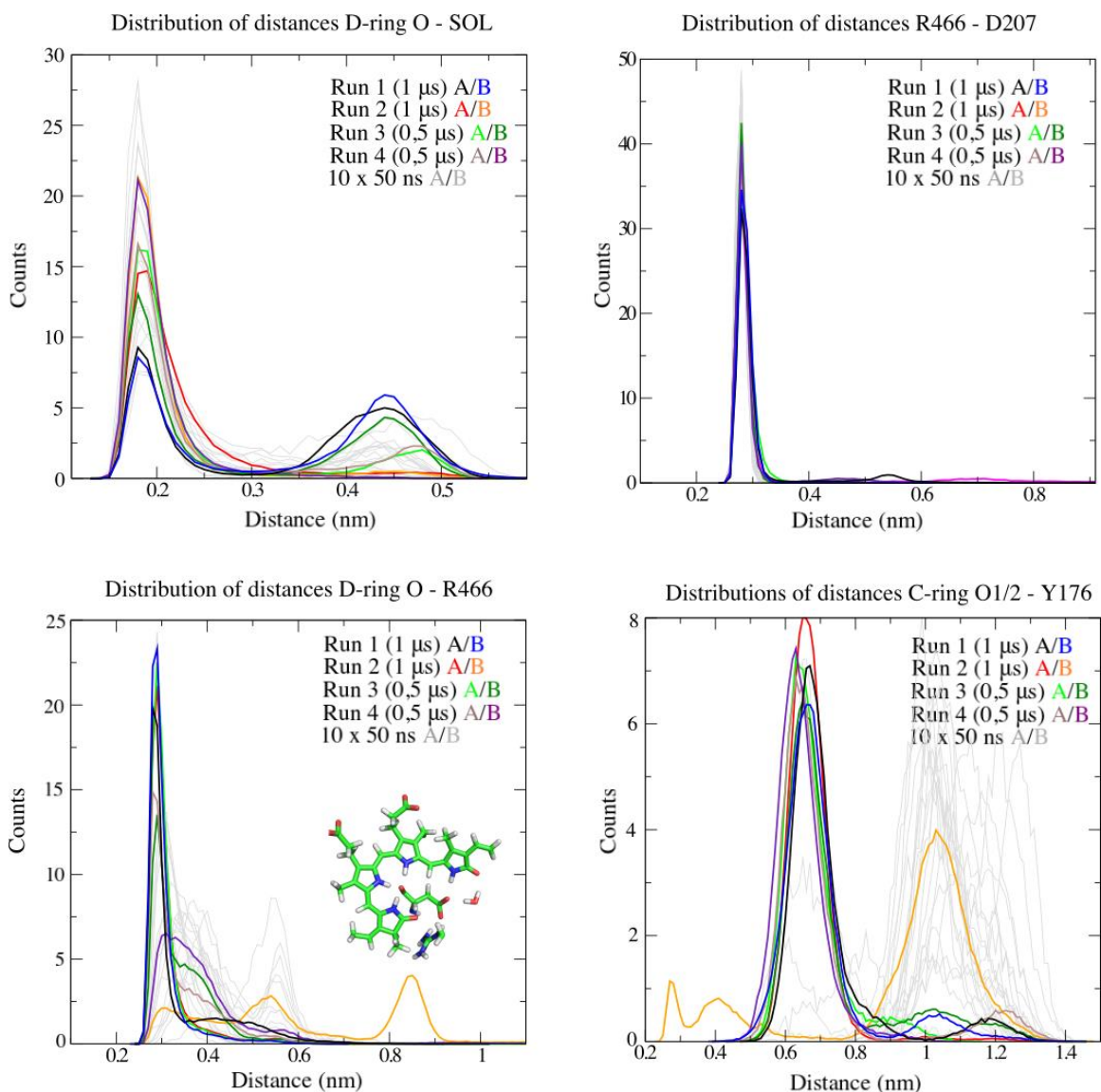


**Figure S13.** Distributions of minimum distances from four longer (runs 1-4) and ten shorter (gray) MD simulations of the Lumi-R state. Minimum distances were calculated between solvent and D-ring atom O, R466 (atoms NH1/2) and D207 (atoms OD1/2,) D-ring atom O and R466 (atoms NH1/2), and C-ring atoms O1/2 and Y176 (atom OH). The conformation of monomer B from run 2 at time 500 ns is also shown (biliverdin, D207, R466 (side chain atoms starting at CG) and water in closest proximity of D-ring O).



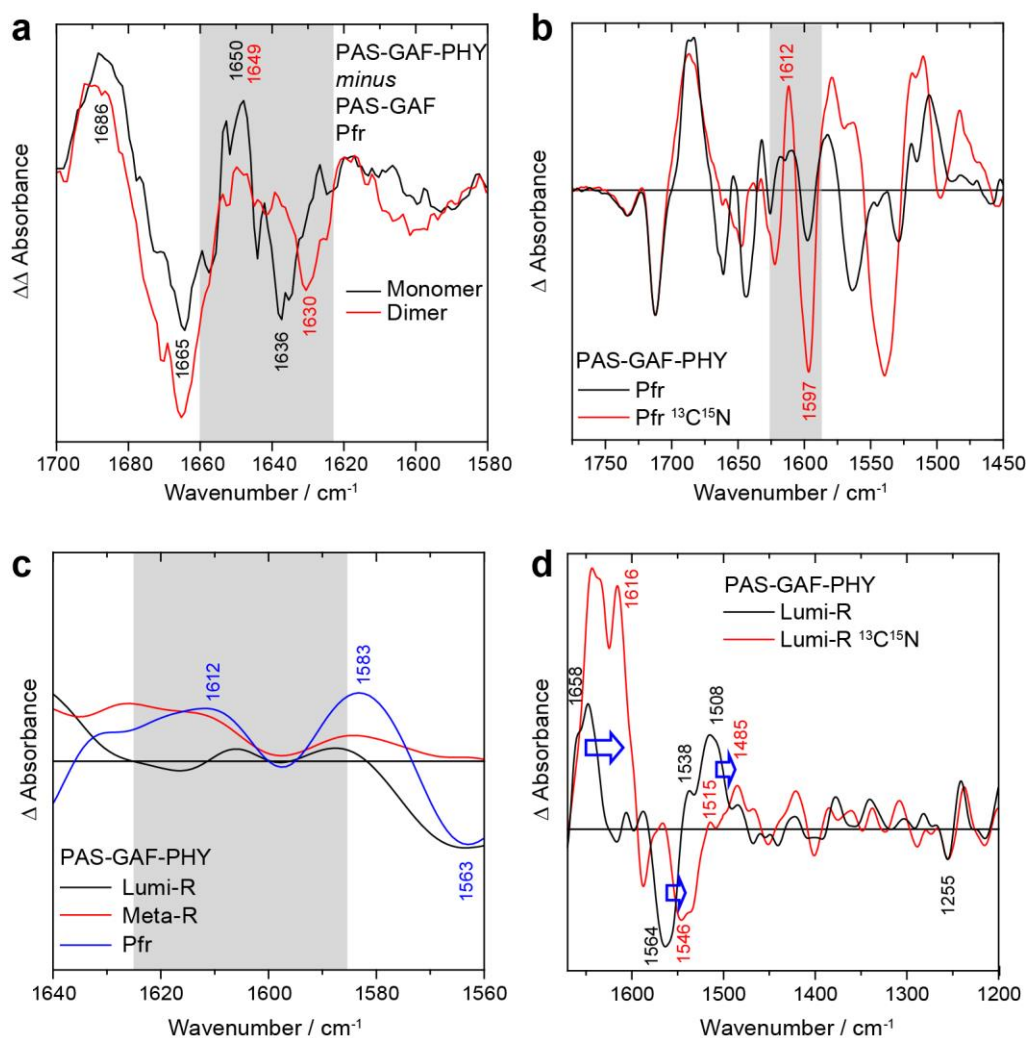


**Figure S14.** FTIR signals of the backbone changes along the photocycle of *DrBphP*<sub>PSM</sub>. (a) An FTIR double difference spectrum of the Pfr *minus* Pr states between PAS-GAF-PHY and PAS-GAF systems. The peak combination at 1636(-) / 1650(+)  $\text{cm}^{-1}$  (1630(-) / 1649(+)  $\text{cm}^{-1}$ ) reveals the  $\beta$ -sheet to  $\alpha$ -helix transition in the PHY domain, presumably in the 'tongue' region. (b) The steady-state Pfr *minus* Pr FTIR spectrum of the PAS-GAF-PHY unit with or without  $^{13}\text{C}^{15}\text{N}$ -labeling. The isotope labeling reveals a clear signal for the  $\beta$ -sheet to  $\alpha$ -helix transition. (c) SADS from the step-scan FTIR experiment of the unlabeled PAS-GAF-PHY. In the spectral region, in which secondary structural changes were observed in the  $^{13}\text{C}^{15}\text{N}$ -labeled system (Figure 5c), small additional contributions from the biliverdin are present. (d) The effect of the  $^{13}\text{C}^{15}\text{N}$  labeling on the amide I and amide II regions on the Lumi-R signal. The shift of the amide I (42  $\text{cm}^{-1}$ ) and amide II (18  $\text{cm}^{-1}$ ) signals confirm that the backbone changes in the Lumi-R in comparison with the Pr state. The scaling of the labeled and unlabeled experiments at 1714  $\text{cm}^{-1}$  is supported by the agreement in intensity of a biliverdin signal at 1255(-)  $\text{cm}^{-1}$ .



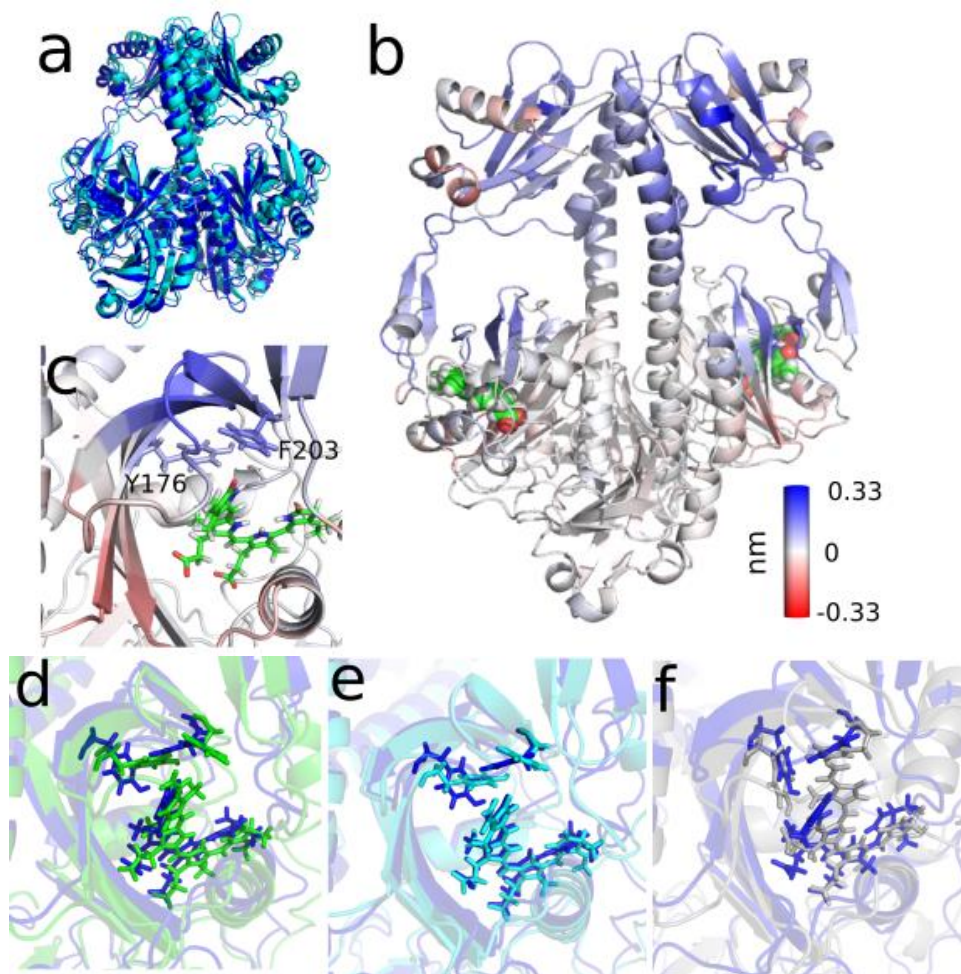


**Figure S15.** The conformational changes in the Lumi-R state. (a) Starting (cyan) and final (blue) conformations from trajectory 1 (1000 ns) of Lumi-R, superimposed on the backbone atoms of residues 20 to 300 (the chromophore binding region of the phytochrome). The backbone is represented as cartoon and the chromophore is shown as spheres. (b) Starting conformation of the Lumi-R simulation, where residues are colored based on the increase (blue) or decrease (red) of the backbone C atom distance from biliverdin, with respect to the Pr simulation. Distances were averaged over the simulation time, and over the A and B monomers. Biliverdin is shown as spheres colored according to atom type (C green, O red, N blue, H white). (c) Chromophore binding region from panel (b). Side chains of Y176 and F203, and biliverdin are indicated with sticks. Colors as in panel (b). (d)-(f) A comparison of the molecular arrangement of the biliverdin and Y176 and F203 after 1000 ns of Lumi-R simulation (blue) with Pr (green), Pr immediately after isomerization (i.e., Lumi-R, 0 ns, cyan) and Pfr (gray). Y176 and F203 are oriented similarly to panel c. Structures are superimposed on the backbone atoms of residues 20 to 300.

## TABLES

**Table S1.** Atomic charges and atom types of Pr and Pfr states of the biliverdin chromophore. Atoms named as in Figure S8.

Atom Name	Atom	Atom Type	Pr state	Pfr state
CBA	C	CT	-0.125784	-0.160213
HBA1	H	HC	0.141099	0.142406
HBA2	H	HC	0.141099	0.142406
CAA	C	CM	-0.128990	-0.150339
HAA	H	HC	0.197467	0.206208
C3A	C	CM	-0.222884	-0.190843
C2A	C	CT	0.150926	0.288527
H2A	H	HC	0.078532	0.035952
CMA	C	CT	-0.232203	-0.257769
HMA1	H	HC	0.071541	0.073841
HMA2	H	HC	0.071541	0.073841
HMA3	H	HC	0.071541	0.073841
C1A	C	C	0.494423	0.431185
0A	O	O	-0.566941	-0.575833
NA	N	NA	-0.371493	-0.213914
HNA	H	H	0.312913	0.212987
C4A	C	CC	0.293610	0.095123
CHB	C	C*	-0.508717	-0.334989
HHB	H	HC	0.180791	0.166613
C1B	C	CC	0.299924	0.152106
C2B	C	C*	0.096990	0.090712
CMB	C	CT	-0.407671	-0.258848
HMB1	H	HC	0.137772	0.085754
HMB2	H	HC	0.137772	0.085754
HMB3	H	HC	0.137772	0.085754
C3B	C	C*	-0.223157	-0.107975
C4B	C	CC	0.204458	0.019292
NB	N	NA	-0.461834	-0.330574
HNB	H	H	0.294567	0.281417
CAB	C	CT	-0.049467	0.011177
HAB1	H	HC	0.059532	0.037059
HAB2	H	HC	0.059532	0.037059
CBB	C	CT	-0.147753	0.005539
HBB1	H	HC	0.032167	-0.024865
HBB2	H	HC	0.032167	-0.024865
CGB	C	C	0.868953	0.836315
O1B	O	O2	-0.799804	-0.804384
O2B	O	O2	-0.799804	-0.804384

CHC	C	CC	-0.300568	-0.131675
HHC	H	HC	0.260852	0.208094
C1C	C	C*	0.338657	0.083961
NC	N	NA	-0.715401	-0.519627
HNC	H	H	0.429492	0.392200
C4C	C	CC	0.575162	0.258241
C3C	C	CC	-0.059559	0.012488
CMC	C	CT	-0.354912	-0.425555
HMC1	H	HC	0.120436	0.133515
HMC2	H	HC	0.120436	0.133515
HMC3	H	HC	0.120436	0.133515
C2C	C	C*	-0.098782	0.125036
CAC	C	CT	0.098471	-0.064168
HAC1	H	HC	0.018879	0.041743
HAC2	H	HC	0.018879	0.041743
CBC	C	CT	-0.201235	-0.030445
HBC1	H	HC	0.032777	-0.007975
HBC2	H	HC	0.032777	-0.007975
CGC	C	C	0.928626	0.850120
O1C	O	O2	-0.830879	-0.749769
O2C	O	O2	-0.830879	-0.749769
CHD	C	CC	-0.591351	-0.399765
HHD	H	HC	0.186294	0.187392
C1D	C	C*	0.429679	0.346411
ND	N	NA	-0.756385	-0.790471
HND	H	H	0.492973	0.441957
C4D	C	C	0.802707	0.814382
OD	O	O	-0.574791	-0.621731
C3D	C	CC	-0.088126	-0.068393
C2D	C	C*	0.009894	0.010889
CMD	C	CT	-0.304626	-0.244646
HMD1	H	HC	0.107849	0.110513
HMD2	H	HC	0.107849	0.110513
HMD3	H	HC	0.107849	0.110513
CAD	C	CM	-0.168161	-0.173485
HAD	H	HC	0.160099	0.173013
CBD	C	CM	-0.373148	-0.418324
HBD1	H	HC	0.185031	0.191871
HBD2	H	HC	0.185031	0.191871

**Table S2.** Atomic charges and atom types of Pr and Pfr states of the Cys24 bound to biliverdin.

Atom name	Atom	Atom type	Pr	Pfr
<b>N</b>	N	N	-0.406250	-0.406250
<b>H</b>	H	H	0.276625	0.276625
<b>CA</b>	C	CT	0.000000	0.000000
<b>HA</b>	H	H1	0.081325	0.081325
<b>CB</b>	C	CT	-0.209278	-0.199281
<b>HB1</b>	H	H1	0.163720	0.155258
<b>HB2</b>	H	H1	0.163720	0.155258
<b>SG</b>	S	S	-0.251045	-0.268582
<b>C</b>	C	C	-0.606750	-0.606750
<b>O</b>	O	O	-0.558450	-0.558450

## SUPPLEMENTARY REFERENCES

- (1) Takala, H.; Niebling, S.; Berntsson, O.; Björling, A.; Lehtivuori, H.; Häkkänen, H.; Panman, M.; Gustavsson, E.; Hoernke, M.; Newby, G.; Zontone, F.; Wulff, M.; Menzel, A.; Ihalainen, J. A.; Westenhoff, S. Light-Induced Structural Changes in a Monomeric Bacteriophytochrome. *Struct. Dyn.* **2016**, *3* (5), 054701.
- (2) Lehtivuori, H.; Rissanen, I.; Takala, H.; Bamford, J.; Tkachenko, N. V.; Ihalainen, J. A. Fluorescence Properties of the Chromophore-Binding Domain of Bacteriophytochrome from *Deinococcus Radiodurans*. *J. Phys. Chem. B* **2013**, *117* (38), 11049–11057.
- (3) Pedersen, A.; Hellberg, K.; Enberg, J.; Karlsson, B. G. Rational Improvement of Cell-Free Protein Synthesis. *N. Biotechnol.* **2011**, *28* (3), 218–224.
- (4) Björling, A.; Berntsson, O.; Lehtivuori, H.; Takala, H.; Hughes, A. J.; Panman, M.; Hoernke, M.; Niebling, S.; Henry, L.; Henning, R.; Kosheleva, I.; Chukharev, V.; Tkachenko, N. V.; Menzel, A.; Newby, G.; Khakhulin, D.; Wulff, M.; Ihalainen, J. A.; Westenhoff, S. Structural Photoactivation of a Full-Length Bacterial Phytochrome. *Sci. Adv.* **2016**, *2* (8), e1600920.
- (5) Thöing, C.; Oldemeyer, S.; Kottke, T. Microsecond Deprotonation of Aspartic Acid and Response of the  $\alpha/\beta$  Subdomain Precede C-Terminal Signaling in the Blue Light Sensor Plant Cryptochrome. *JACS* **2015**, *137* (18), 5990–5999.
- (6) Covington, A. K.; Paabo, M.; Robinson, R. A.; Bates, R. G. Use of the Glass Electrode in Deuterium Oxide and the Relation between the Standardized PD (PaD) Scale and the Operational PH in Heavy Water. *Anal. Chem.* **1968**, *40* (4), 700–706.
- (7) Bredenbeck, J.; Hamm, P. Versatile Small Volume Closed-Cycle Flow Cell System for Transient Spectroscopy at High Repetition Rates. *Rev. Sci. Instrum.* **2003**, *74* (6), 3188–3189.
- (8) Maçôas, E. M. S.; Kananavicius, R.; Myllyperkiö, P.; Pettersson, M.; Kunttu, H. Ultrafast Electronic and Vibrational Energy Relaxation of Fe(Acetylacetonate)<sub>3</sub> in Solution. *J. Phys. Chem. A* **2007**, *111* (11), 2054–2061.
- (9) Hamm, P.; Kaindl, R. A.; Stenger, J. Noise Suppression in Femtosecond Mid-Infrared Light Sources. *Opt. Lett.* **2000**, *25* (24), 1798.
- (10) Lenngren, N.; Edlund, P.; Takala, H.; Stucki-Buchli, B.; Rumfeldt, J.; Peshev, I.; Häkkänen, H.; Westenhoff, S.; Ihalainen, J. A. Coordination of the Biliverdin D-Ring in Bacteriophytochromes. *Phys. Chem. Chem. Phys.* **2018**, *20* (27), 18216–18225.
- (11) Berendsen, H. J. C.; van der Spoel, D.; van Drunen, R. GROMACS: A Message-Passing Parallel Molecular Dynamics Implementation. *Comput. Phys. Commun.* **1995**, *91* (1–3), 43–56.
- (12) Juréus, A.; Langel, Ü. Galanin and Galanin Antagonists. *Acta Chim. Slov.* **1996**, *43* (1), 51–60.
- (13) Van Der Spoel, D.; Lindahl, E.; Hess, B.; Groenhof, G.; Mark, A. E.; Berendsen, H. J. C. GROMACS: Fast, Flexible, and Free. *J. Comput. Chem.* **2005**, *26* (16), 1701–1718.
- (14) Hess, B.; Kutzner, C.; Van Der Spoel, D.; Lindahl, E. GROMACS 4: Algorithms for

- Highly Efficient, Load-Balanced, and Scalable Molecular Simulation. *J. Chem. Theory Comput.* **2008**, 4 (3), 435–447.
- (15) Burgie, E. S.; Wang, T.; Bussell, A. N.; Walker, J. M.; Li, H.; Vierstra, R. D. Crystallographic and Electron Microscopic Analyses of a Bacterial Phytochrome Reveal Local and Global Rearrangements during Photoconversion. *J. Biol. Chem.* **2014**, 289 (35), 24573–24587.
  - (16) Burgie, E. S.; Zhang, J.; Vierstra, R. D. Crystal Structure of Deinococcus Phytochrome in the Photoactivated State Reveals a Cascade of Structural Rearrangements during Photoconversion. *Structure* **2016**, 24 (3), 448–457.
  - (17) Sali, A.; Blundell, T. L. Comparative Protein Modelling by Satisfaction of Spatial Restraints. *J. Mol. Biol.* **1993**, 234 (3), 779–815.
  - (18) Fiser, A.; Sali, A. ModLoop: Automated Modeling of Loops in Protein Structures. *Bioinformatics* **2003**, 19 (18), 2500–2501.
  - (19) Duan, Y.; Wu, C.; Chowdhury, S.; Lee, M. C.; Xiong, G.; Zhang, W.; Yang, R.; Cieplak, P.; Luo, R.; Lee, T.; Caldwell, J.; Wang, J.; Kollman, P. A Point-Charge Force Field for Molecular Mechanics Simulations of Proteins Based on Condensed-Phase Quantum Mechanical Calculations. *J. Comput. Chem.* **2003**, 24 (16), 1999–2012.
  - (20) Jorgensen, W. L.; Chandrasekhar, J.; Madura, J. D.; Impey, R. W.; Klein, M. L. Comparison of Simple Potential Functions for Simulating Liquid Water. *J. Chem. Phys.* **1983**, 79 (2), 926–935.
  - (21) Bayly, C. I.; Cieplak, P.; Cornell, W. D.; Kollman, P. A. A Well-Behaved Electrostatic Potential Based Method Using Charge Restraints for Deriving Atomic Charges: The RESP Model. *J. Phys. Chem.* **1993**, 97 (40), 10269–10280.
  - (22) Darden, T.; York, D.; Pedersen, L. Particle Mesh Ewald: An N·log(N) Method for Ewald Sums in Large Systems. *J. Chem. Phys.* **1993**, 98 (12), 10089–10092.
  - (23) Essmann, U.; Perera, L.; Berkowitz, M. L.; Darden, T.; Lee, H.; Pedersen, L. G. A Smooth Particle Mesh Ewald Method. *J. Chem. Phys.* **1995**, 103 (19), 8577–8593.
  - (24) Berendsen, H. J. C.; Postma, J. P. M.; Van Gunsteren, W. F.; Dinola, A.; Haak, J. R. Molecular Dynamics with Coupling to an External Bath. *J. Chem. Phys.* **1984**, 81 (8), 3684–3690.
  - (25) Bussi, G.; Donadio, D.; Parrinello, M. Canonical Sampling through Velocity Rescaling. *J. Chem. Phys.* **2007**, 126 (1), 14101.
  - (26) Miyamoto, S.; Kollman, P. A. Settle: An Analytical Version of the SHAKE and RATTLE Algorithm for Rigid Water Models. *J. Comput. Chem.* **1992**, 13 (8), 952–962.
  - (27) Hess, B.; Bekker, H.; Berendsen, H. J. C.; Fraaije, J. G. E. M. LINCS: A Linear Constraint Solver for Molecular Simulations. *J. Comput. Chem.* **1997**, 18 (12), 1463–1472.
  - (28) Zwanzig, R. W. High Temperature Equation of State by a Perturbation Method. I. Nonpolar Gases. *J. Chem. Phys.* **1954**, 22 (8), 1420–1426.
  - (29) Andresen, M.; Wahl, M. C.; Stiel, A. C.; Grater, F.; Schafer, L. V.; Trowitzsch, S.; Weber, G.; Eggeling, C.; Grubmüller, H.; Hell, S. W.; Jakobs, S. Structure and Mechanism of the Reversible Photoswitch of a Fluorescent Protein. *PNAS* **2005**, 102 (37), 13070–13074.

- (30) Takala, H.; Björling, A.; Berntsson, O.; Lehtivuori, H.; Niebling, S.; Hoernke, M.; Kosheleva, I.; Henning, R.; Menzel, A.; Ihalainen, J. A.; Westenhoff, S. Signal Amplification and Transduction in Phytochrome Photosensors. *Nature* **2014**, *509* (7499), 245–248.
- (31) Rockwell, N. C.; Shang, L.; Martin, S. S.; Lagarias, J. C. Distinct Classes of Red/Far-Red Photochemistry within the Phytochrome Superfamily. *PNAS* **2009**, *106* (15), 6123–6127.
- (32) Humphrey, W.; Dalke, A.; Schulten, K. VMD: Visual Molecular Dynamics. *J. Mol. Graph.* **1996**, *14* (1), 33–38.
- (33) Fried, S. D.; Bagchi, S.; Boxer, S. G. Measuring Electrostatic Fields in Both Hydrogen-Bonding and Non-Hydrogen-Bonding Environments Using Carbonyl Vibrational Probes. *JACS* **2013**, *135* (30), 11181–11192.
- (34) Zhang, J.; Chen, P.; Yuan, B.; Ji, W.; Cheng, Z.; Qiu, X. Real-Space Identification of Intermolecular Bonding with Atomic Force Microscopy. *Science* **2013**, *342* (6158), 611–614.
- (35) Foerstendorf, H.; Benda, C.; Gärtner, W.; Storf, M.; Scheer, H.; Siebert, F. FTIR Studies of Phytochrome Photoreactions Reveal the C=O Bands of the Chromophore: Consequences for Its Protonation States, Conformation, and Protein Interaction. *Biochemistry* **2001**, *40* (49), 14952–14959.
- (36) Haris, P. I.; Robillard, G. T.; Van Dijk, A. A.; Chapman, D. Potential of Carbon-13 and Nitrogen-15 Labeling for Studying Protein-Protein Interactions Using Fourier-Transform Infrared Spectroscopy. *Biochemistry* **1992**, *31* (27), 6279–6284.
- (37) Frisch, M. J.; Trucks, G. W.; Schlegel, H. B.; Scuseria, G. E.; Robb, M. A.; Cheeseman, J. R.; Scalmani, G.; Barone, V.; Petersson, G. A.; Nakatsuji, H.; Li, X.; Caricato, M.; Marenich, A. V.; Bloino, J.; Janesko, B. G.; Gomperts, R.; Mennucci, B.; Hratchian, H. P.; Ortiz, J. V.; Izmaylov, A. F.; Sonnenberg, J. L.; Williams-Young, D.; Ding, F.; Lipparini, F.; Egidi, F.; Goings, J.; Peng, B.; Petrone, A.; Henderson, T.; Ranasinghe, D.; Zakrzewski, V. G.; Gao, J.; Rega, N.; Zheng, G.; Liang, W.; Hada, M.; Ehara, M.; Toyota, K.; Fukuda, R.; Hasegawa, J.; Ishida, M.; Nakajima, T.; Honda, Y.; Kitao, O.; Nakai, H.; Vreven, T.; Throssell, K.; Montgomery Jr., J. A.; Peralta, J. E.; Ogliaro, F.; Bearpark, M. J.; Heyd, J. J.; Brothers, E. N.; Kudin, K. N.; Staroverov, V. N.; Keith, T. A.; Kobayashi, R.; Normand, J.; Raghavachari, K.; Rendell, A. P.; Burant, J. C.; Iyengar, S. S.; Tomasi, J.; Cossi, M.; Millam, J. M.; Klene, M.; Adamo, C.; Cammi, R.; Ochterski, J. W.; Martin, R. L.; Morokuma, K.; Farkas, O.; Foresman, J. B.; Fox, D. J. Gaussian03 Revision C.02. 2009.